Dalton Transactions

ROYAL SOCIETY OF CHEMISTRY

PAPER

View Article Online
View Journal | View Issue

Check for updates

Cite this: *Dalton Trans.*, 2020, **49**, 17779

Multi-peaked broad-band red phosphor $Y_3Si_6N_{11}$:Pr^{3+} for white LEDs and temperature sensing†

Dashuai Sun, [a,b] Liangliang Zhang, *[a] Zhendong Hao, [a] Hao Wu, [a] Huajun Wu, [a] Yongshi Luo,[a] Lin Yang,[a,b] Xia Zhang,[a] Feng Liu [c] and Jiahua Zhang *[a,b]

Received 12th October 2020,
Accepted 16th November 2020

DOI: 10.1039/d0dt03532g

rsc.li/dalton

The indispensable broad-band red phosphors for LED lighting generally show a long emission tail for wavelengths longer than 650 nm, which consumes excitation energy but contributes little luminance. Here, we report, for the first time, a broad red emission band with a steep falling edge at 652 nm, formed of widely distributed $^1D_2 \rightarrow {}^3H_4$ emission lines of Pr^{3+} in $Y_3Si_6N_{11}$ due to a large Stark splitting of the $^3H_4$ (930 cm^{-1}) and $^1D_2$ (725 cm^{-1}) levels. The red emission exhibits a 43 nm bandwidth, which is the widest in Pr^{3+}-doped phosphors reported so far. The red $Y_3Si_6N_{11}$:Pr^{3+} phosphor was applied for the fabrication of 310 nm UV chip-based white LEDs, and a high color rendering index of 96 at a low correlated color temperature of 4188 K was achieved. Furthermore, a temperature-sensing scheme was proposed based on the temperature-dependent intensity ratios of the emission lines from the thermally coupled and large Stark splitting levels of the $^1D_2$ state. Relative sensitivities as a function of temperature were studied in the range of 93–473 K. The findings of this study indicate that $Y_3Si_6N_{11}$:Pr^{3+} is an attractive broad-band red phosphor for both high color rendering white LEDs and temperature sensing applications.

1. Introduction

The white light-emitting diodes (WLEDs) fabricated by combining a blue LED chip with yellow phosphor $Y_3Al_5O_{12}$:Ce^{3+} (YAG:Ce^{3+}) suffer from a low colour rendering index (CRI < 80) due to the lack of red component.[1–14] The (Ca,Sr)$AlSiN_3$:Eu^{2+} and $(Ba,Sr)_2Si_5N_8$:Eu^{2+} red broad-band phosphors have been widely used in WLEDs for improving the CRI.[15–20] However, the red phosphors show a long emission tail for wavelengths longer than 650 nm, which consumes excitation energy but contributes little luminance.[21–23] Pr^{3+} ions are a well-known red luminescence centre for the $^1D_2 \rightarrow {}^3H_4$ transition, and a large number of Pr^{3+}-doped red phosphors have been developed, including $Y_3Al_5O_{12}$:Pr^{3+},[24,25] $Ca_3Sc_2Si_3O_{12}$:Pr^{3+},[26] $LaBMO_6$:Pr^{3+},[27] β-SiAlON:Pr^{3+},[28,29] $YInGe_2O_7$:Pr^{3+},[30] $Ca_{19}Mg_2(PO_4)_{14}$:Pr^{3+},[31] and $BaMoO_4$:Pr^{3+}.[32] Unfortunately, all these phosphors show narrow-band emission with a bandwidth of only a few nanometers, which cannot effectively supplement the red spectral components of WLEDs. In order to solve the problem, we propose a strategy for obtaining red broad-band tailless emission, originating from the $^1D_2 \rightarrow {}^3H_4$ transition of Pr^{3+} by finding a suitable matrix to achieve a large Stark splitting of the $^1D_2$ and $^3H_4$ levels of Pr^{3+}.

Due to the effect of the crystal field and the symmetry of the surrounding environment, the energy levels of the rare-earth ions can be split to different degrees. The lower the symmetry, the more the degeneracy of the energy levels can be lifted, and more Stark levels can be generated.[33–35] In our previous study, we reported a broad-band yellow phosphor $Y_3Si_6N_{11}$:Ce^{3+} (YSN:Ce^{3+}), and the microstructure of $Y_3Si_6N_{11}$ was studied in detail *via* Rietveld structural refinement.[36] There were two different Y lattice sites. When an activator ion with a larger radius than the Y^{3+} ion is introduced, it will tend to occupy the larger space but worse symmetry Y1 lattice site. On this basis, we synthesized the YSN:Pr^{3+} phosphor.

In this study, for the first time, we found a red broad-band tailless emission of Pr^{3+} in the YSN matrix. The photoluminescence (PL) properties of YSN:Pr^{3+} were studied. The red broad-band was revealed to originate from the combination of the transitions from the large Stark splitting levels of $^1D_2$ to that of $^3H_4$. The red emission band was employed for the fabrication of 310 nm UV chip-based white LEDs, and a high color rendering index at a low correlated color temperature was achieved. Furthermore, the multi-peaked red emis-

[a]State Key Laboratory of Luminescence and Applications, Changchun Institute of Optics, Fine Mechanics and Physics, Chinese Academy of Sciences, Changchun 130033, China. E-mail: zhangliangliang@ciomp.ac.cn, zhangjh@ciomp.ac.cn
[b]Center of Materials Science and Optoelectronics Engineering, University of Chinese Academy of Sciences, Beijing 100049, China
[c]Key Laboratory for UV-Emitting Materials and Technology of Ministry of Education, Northeast Normal University, Changchun 130024, China

†Electronic supplementary information (ESI) available. See DOI: 10.1039/d0dt03532g

sion band showed a temperature-dependent fluorescence intensity ratio (FIR) of the emission peaks due to the thermally coupled Stark levels of the $^1D_2$ state. Thus, a strategy for optical thermometry based on the FIR technique was proposed for the YSN:Pr^{3+} phosphor.

2. Experimental section

2.1. Materials and preparation

The $Y_3Si_6N_{11}$:Ce^{3+} samples were synthesized *via* a solid-state reaction method. Y_2O_3 (4 N), PrF_3 (4 N), α-Si_3N_4 (Alfa Aesar), and $C_2H_4N_4$ (C.P.) were weighed stoichiometrically, and AlF_3 (C.P.) was added as a fluxing agent. All the starting materials were ground thoroughly in an agate mortar. The mixtures were transferred into a graphite crucible heated at 210 °C for 1 h and then sintered at 1600 °C for 5 h under N_2 atmosphere at a heating speed of 3 °C min^{-1}, followed by cooling to room temperature in a furnace. The samples were then taken out from the graphite crucible and reground into fine powders and were subsequently put into an alumina crucible heated at 600 °C for 6 h in air to remove the excess carbon.

2.2. Measurement and characterization

The powder X-ray diffraction (XRD) patterns of all samples were collected on a Bruker D8 Focus diffractometer in the 2θ range from 15° to 65° with Cu Kα radiation (λ = 1.54056 Å) operated at 40 kV and 30 mA, and the XRD data were collected with a step size of 0.02° and count time of 0.2 s per step. The structure refinement was carried out by the Rietveld method using the FullProf program. The photoluminescence (PL) and photoluminescence excitation (PLE) spectra were recorded using an FLS920 spectrometer (Edinburgh Instruments, U.K.). In fluorescence lifetime measurements, an optical parametric oscillator (OPO) was used as an excitation source, and the signal was detected by a Tektronix digital oscilloscope (TDS 3052). Fluorescence microscope PL images were recorded on an Olympus BX53MTRF-S optical microscope, and the temperature-dependent PL spectra were measured on a Olympus BX53MTRF-S optical microscope with an external heater and an Ocean optics micro-spectrometer. The optical properties of the fabricated w-LEDs were measured using an integrated sphere spectroradiometer system (LHS-1000, Everfine Co., Hangzhou, China).

3. Results and discussion

3.1. Structural properties

The crystalline phase purities of the as-prepared powder sample were examined *via* XRD at room temperature. Fig. 1(a) shows the XRD patterns of YSN:$x$$Pr^{3+}$ (x = 2‰–12‰) samples, and the calculated XRD pattern from the Rietveld structural refinement is also shown for comparison. We can see that all the samples exhibit almost similar XRD patterns, and no obvious different peaks were detected. This indicates that the samples obtained *via* a solid-state reaction method in this study were of single phase, and Pr^{3+} ions were completely dissolved in the host while keeping the crystal structure intact. The Rietveld structural refinement of YSN:8‰Pr^{3+} was performed to understand the microstructure. The Rietveld R-factors, R_p and R_{wp}, were converged to 8.40% and 8.89%,

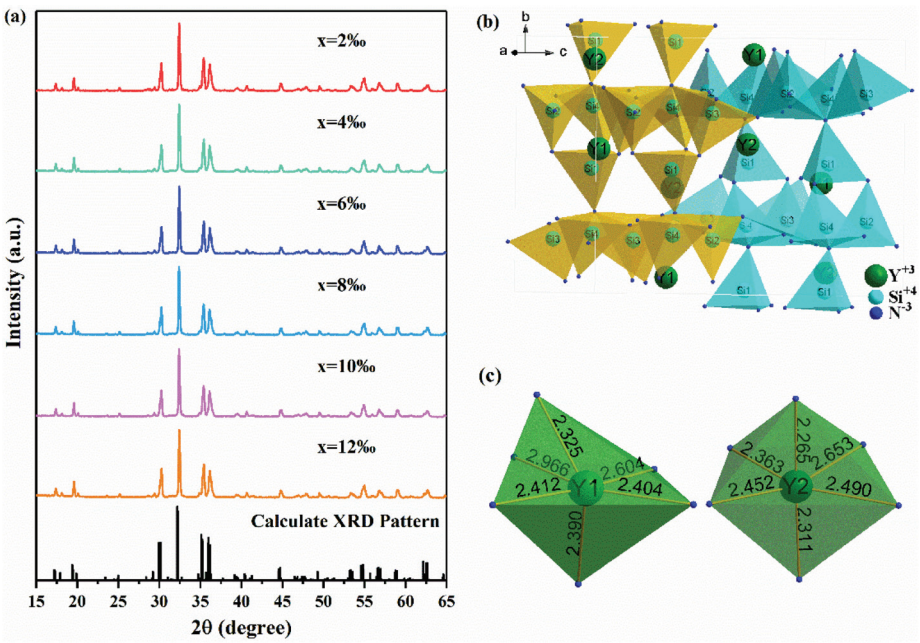

Fig. 1 The XRD patterns of YSN:$x$$Pr^{3+}$ (x = 2‰–12‰) samples and calculated XRD pattern, (b) the crystal structure of YSN, (c) the coordination environment of the Y1 site and Y2 site.

respectively. The observed, calculated, and different patterns of the XRD refinement of YSN:8‰Pr^{3+} are shown in Fig. S1.† The crystal lattice parameters are listed in Table S1.† The atomic coordinates are listed in Table S2.†

As illustrated in Fig. 1b, there are four Si sites (Si1, Si2, Si3, and Si4), and each Si atom is connected to four N atoms to form a condensed [SiN_4] tetrahedron. Four different [SiN_4] tetrahedrons form a star-like unit [$N(SiN_3)_4$] by sharing vertex N7, and these units are alternately stacked into two types of layers with opposite directions. There are two Y sites (Y1 and Y2) which are all coordinated with six N^{3-} ions, as shown in Fig. 1c. The Y^{3+}–N^{3-} average bond length is found to be 2.517 Å at the Y1 site and 2.422 Å at the Y2 site. Although both ligand polyhedra are twisted octahedrons, the Y1 ligand polyhedron is more twisted than the Y2 ligand polyhedron. In general, the Y1 site had a larger space and worse symmetry.

3.2. Luminescence properties

The blue dot line in Fig. 2(c) is the luminosity function, which indicates the sensitivity of the human eye to light of different wavelengths. It can be seen that the human eye is extremely insensitive to light with a wavelength greater than 650 nm. The PL spectrum of YSN:8‰Pr^{3+} under 303 nm excitation and PL spectrum of $CaAlSiN_3$:Eu^{2+} under 460 nm excitation are shown in Fig. 2(c). Both YSN:8‰Pr^{3+} and $CaAlSiN_3$:Eu^{2+} exhibit a wide red emission band with the same central wavelength. However, unlike the wide emission band with a long tail over 650 nm derived from the 5d → 4f electron transition in $CaAlSiN_3$:Eu^{2+}, the YSN:8‰Pr^{3+} red broad-band with a steep falling edge at 652 nm was formed by the superposition of multiple line peaks derived from the 4f → 4f electronic transition. The fluorescence microscopy PL images of YSN:8‰Pr^{3+} and $CaAlSiN_3$:Eu^{2+} are also presented in Fig. 2(a) and (b), respectively. It is clear that the particle size and emission color of YSN:8‰Pr^{3+} were similar to those of the commercial red phosphor $CaAlSiN_3$:Eu^{2+}.

To illustrate the potential of the Pr^{3+} multi-peaked broad-band for application, the WLED in Fig. 3(a) was fabricated using a 310 nm LED chip, with a blend of blue phosphor BAM:Eu^{2+} and yellow phosphor YSN:2%Ce^{3+}, as reported previously,[36] and the WLED in Fig. 3(b) was fabricated using a 310 nm LED chip, with a blend of blue phosphor BAM:Eu^{2+}, yellow phosphor YSN:2%Ce^{3+}, and the red phosphor YSN:8‰Pr^{3+}. Comparing the two WLEDs, the CCT of the WLED reduced from 5853 k to 4188 k, and CRI increased from 81.4 to 96 by adding the red broad-band YSN:Pr^{3+} phosphor. The efficiency of the white LED was about 1 lm W^{-1}. The low luminous efficiency was due to the low efficiency of the 310 nm LED chip and the lack of synthesis optimization of the YSN:Pr^{3+} phosphor. YSN:Pr^{3+} provides a new strategy for developing new red broad-band tailless emission phosphors. Therefore, it is of great significance to understand the origin of the red broad-band emission of Pr^{3+} in YSN.

Fig. 4(a) shows the PL spectra of YSN:$x$$Pr^{3+}$ (x = 2‰–12‰) under 303 nm excitation, and the highest PL intensity of YSN:Pr^{3+} appeared at a Pr^{3+} concentration of 8‰. The PLE spectrum of YSN:8‰ Pr^{3+} monitored at 648 nm is presented in Fig. 4(b), and the inset is a larger version of the red box area. The PLE band at 303 nm belongs to the 4f → 5d transition of

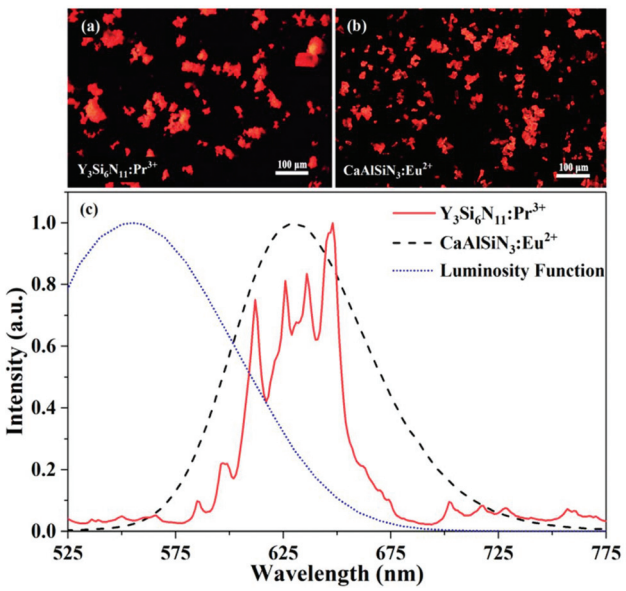

Fig. 2 (a) Fluorescence microscopy PL image of YSN:8‰Pr^{3+} under 303 nm excitation, (b) fluorescence microscopy PL image of $CaAlSiN_3$:Eu^{2+} under 460 nm excitation, (c) the luminosity function, PL spectrum of YSN:8‰Pr^{3+} under 303 nm excitation, and PL spectrum of $CaAlSiN_3$:Eu^{2+} under 460 nm excitation.

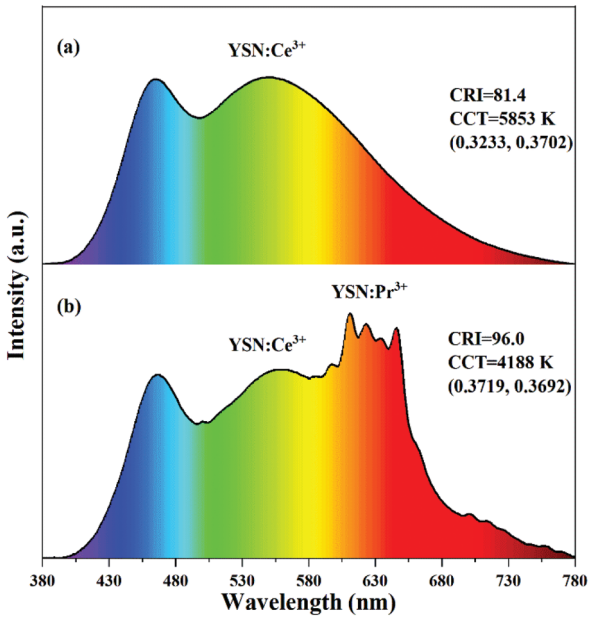

Fig. 3 (a) The PL spectrum of the top pc-WLED fabricated with BAM:Eu^{2+} and YSN:Ce^{3+} on a 310 nm chip under a current of 100 mA, (b) the PL spectrum of the lower pc-WLED fabricated with BAM:Eu^{2+},YSN:Ce^{3+}, and YSN:Pr^{3+} on a 310 nm chip under a current of 100 mA.

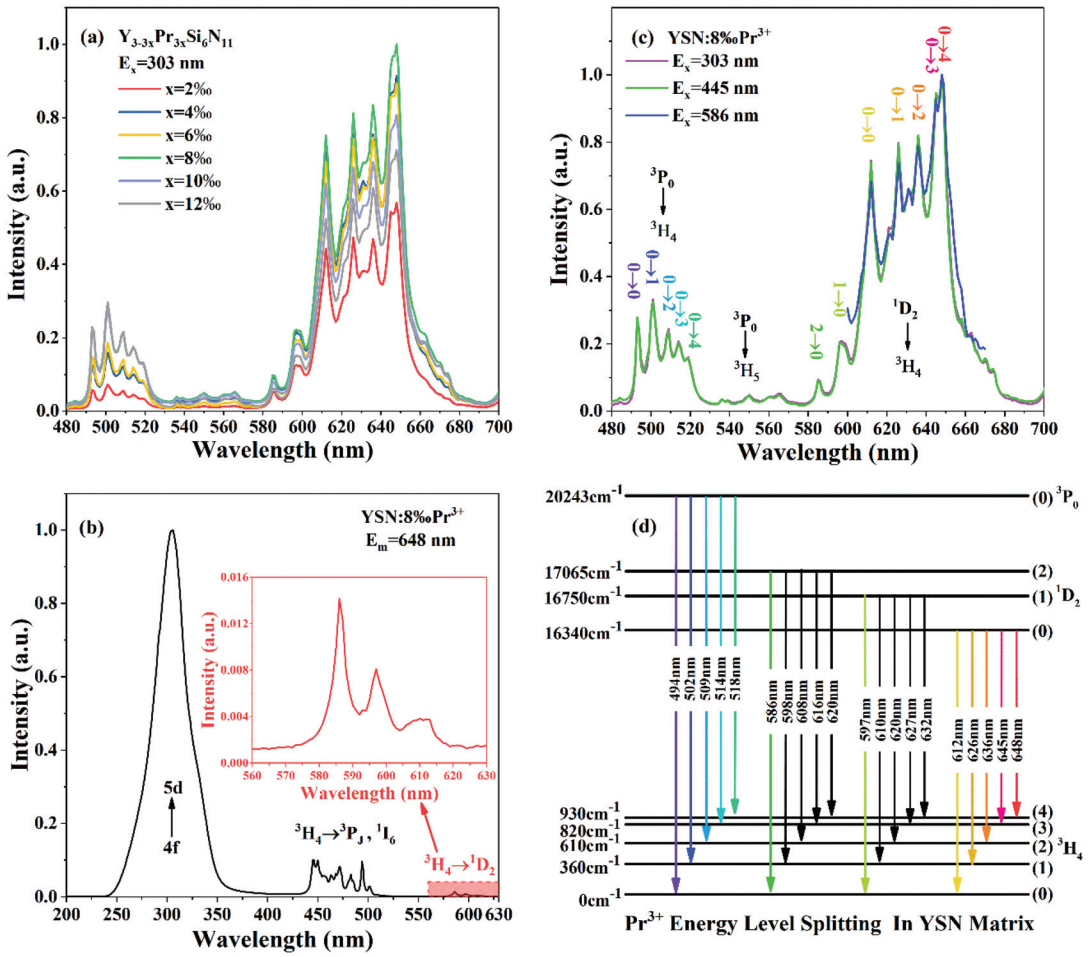

Fig. 4 (a) The PL spectra of YSN:xPr^{3+} (x = 2‰–12‰) under 303 nm excitation, (b) the PLE spectrum of YSN:8‰Pr^{3+} monitored at 648 nm, (c) the PL spectra of YSN:8‰Pr^{3+} under the excitation of 303 nm, 445 nm and 586 nm, (d) the Pr^{3+} energy level splitting diagram in YSN.

Pr^{3+}. Moreover, the series of PLE peaks located within 445–502 nm was attributed to the $^3H_4 \rightarrow {}^3P_J$ and $^3H_4 \rightarrow {}^1I_6$ transition of Pr^{3+}, and the three PLE peaks in the red box area were assigned to the $^3H_4 \rightarrow {}^1D_2$ transition of Pr^{3+}. Correspondingly, the PL spectra under the excitation of 303 nm, 445 nm, and 586 nm were measured and are shown in Fig. 4(c). We can see that all the PL spectra are consistent in the range of 600–650 nm. Under the excitation of 586 nm, only $^1D_2$ of Pr^{3+} can be excited. Therefore, all the emission peaks in this red region come from the $^1D_2 \rightarrow {}^3H_4$ transition of Pr^{3+}. As shown in Fig. 4(c), the PL spectrum under the 5d band (303 nm) excitation is exactly the same as that under $^3H_4 \rightarrow {}^3P_2$ (445 nm) excitation. The emission peaks located within 494–518 nm were assigned to the $^3P_0 \rightarrow {}^3H_4$ transition, and the emission peaks located within 535–565 nm were attributed to the $^3P_0 \rightarrow {}^3H_5$ transition.

The analysis of the luminescence decay was also carried out to confirm the assignment of each peak because emission originating from the $^1D_2$ state had a longer lifetime than that of $^3P_0$. Fig. 5(a) and (b) demonstrate the fluorescence decay curves of YSN:8‰Pr^{3+} (after pulse excitation at 303 nm while being monitored at different wavelengths) that correspond to $^3P_0 \rightarrow {}^3H_4$ and $^1D_2 \rightarrow {}^3H_4$, respectively. The fluorescence decay was around 0.4 μs when monitored at 494 nm, 502 nm, 509 nm, 514 nm, 518 nm, and 539 nm, with all these emission peaks being derived from $^3P_0$ of Pr^{3+}. The fluorescence decay was around 31 μs when monitored at 586 nm, 597 nm, 612 nm, 626 nm, 636 nm, and 648 nm, and all these emission peaks were derived from the $^1D_2$ of Pr^{3+}. The assignment of each peak here is consistent with the conclusion given above.

The fluorescence decay curves of YSN:xPr^{3+} (x = 2‰–12‰) after pulse excitation at 303 nm while being monitored at 648 nm are presented in Fig. S2.† With the increase in the Pr^{3+} doping concentration, due to the cross-relaxation process between Pr^{3+} ions *via* the coupling of $^1D_2 \rightarrow {}^1G_4$ relaxation with $^3H_4 \rightarrow {}^3F_4$ excitation, the lifetime gradually reduced from 50 μs to 21 μs. Quantum yield (QY) is an important parameter of phosphor due to the 5d band electrons band entering the conduction band through the photoionization process, cross-relaxation process between Pr^{3+} ions *via* the coupling of $^1D_2 \rightarrow {}^1G_4$ relaxation with $^3H_4 \rightarrow {}^3F_4$ excitation, and the lack of synthesis optimization. The QY of the YSN:Pr^{3+} phosphor was found to be less than 10%.

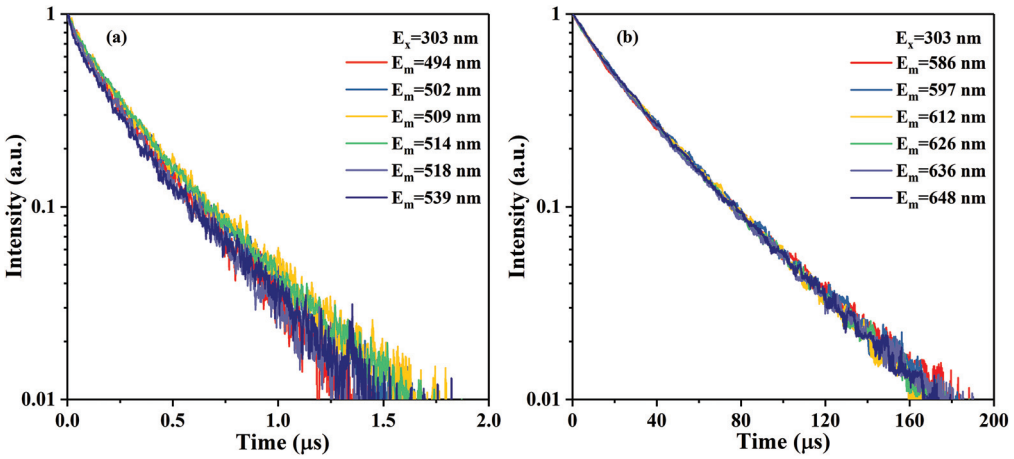

Fig. 5 (a) Fluorescence decay curves of YSN:8‰Pr^{3+} after pulse excitation at 303 nm with the decay being monitored at 494 nm, 502 nm, 509 nm, 514 nm 518 nm, and 539 nm; (b) fluorescence decay curves of YSN:8‰Pr^{3+} after pulse excitation at 303 nm with the decay being monitored at 586 nm, 597 nm, 612 nm, 626 nm, 636 nm, and 648 nm.

Due to the effect of the crystal field and the change in the symmetry of the surrounding environment, $^{2S+1}L_J$ can be split into 2J + 1 Stark levels at most. Since the $^3P_0$ level will not split further, the five $^3P_0 \rightarrow {}^3H_4$ emission peaks located within 494–518 nm imply the five Stark levels of $^3H_4$. The three PLE peaks (586 nm, 597 nm, and 612 nm) in the red box area of Fig. 4(b) and the disappearance of the first two emission peaks at the same position (586 nm and 597 nm) in Fig. 6(a) at 93 K imply the three Stark levels of $^1D_2$. Based on the above analyses, the Pr^{3+} energy level splitting diagram is shown in Fig. 4(d). We can see that the $^1D_2$ split was at 725 cm^{-1} and the $^3H_4$ split was even up to 930 cm^{-1}. This large energy level splitting was related to the asymmetric six coordinated N^{3-} ions around Pr^{3+} ions in the YSN matrix. The colored arrows correspond to the emission peaks that can be directly distinguished in the PL spectrum and were marked with the same color in Fig. 4(c). The black arrows correspond to the emission peaks that were calculated by the determined energy level.

The temperature-dependent PL spectra of YSN:8‰Pr^{3+} under the excitation at 303 nm were measured and are displayed in Fig. 6(a). With the increasing temperature, the $^3P_0 \rightarrow {}^3H_4$ emission peaks located within 494–518 nm keep an unchanged spectral shape, while the $^1D_2 \rightarrow {}^3H_4$ emission peaks located within 586–648 nm show pronounced variation in their relative intensities. As the temperature rises from 93 K to 273 K, the 645 nm and 648 nm emission peaks decrease rapidly, while the 626 nm and 636 nm emission peaks decrease slowly. On the other hand, the intensity of the 612 nm emission peak does not decrease but increases as well as the 586 nm and 597 nm emission peaks appeared and rapidly increased.

These different changes can be well explained by the Pr^{3+} energy level splitting shown in Fig. 4(d). The emission peaks from the Stark level (2) of $^1D_2$ are located within 586–620 nm, the emission peaks from the Stark level (1) of $^1D_2$ are located within 597–632 nm, and the emission peaks from the Stark

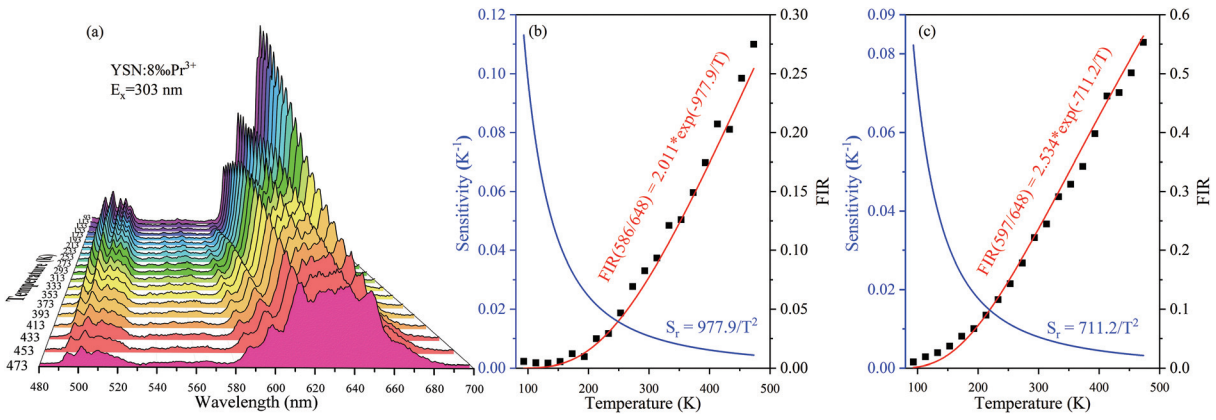

Fig. 6 (a) Temperature-dependent PL spectra of YSN: 8‰Pr^{3+} under 303 nm excitation, (b) the 586 nm and 648 nm emission peaks FIR and relative sensitivity as a function of absolute temperature, (c) the 597 nm and 648 nm emission peaks FIR and relative sensitivity as a function of absolute temperature.

level (0) of $^1D_2$ were located within 612–648 nm. The 586 nm and 597 nm emission peaks, which are derived from the transition of the upper Stark level of $^1D_2$, cannot be observed at 93 K, indicating that the upper Stark level of $^1D_2$ is almost empty at 93 K. Moreover, the observed five peaks, 612 nm, 626 nm, 636 nm, 645 nm, and 648 nm, reflect the transitions from the lowest Stark level (0) of $^1D_2$ to the five Stark levels of $^3H_4$.

As the temperature gradually increased from 93 K to 273 K, the upper Stark levels (1) and (2) of $^1D_2$ are thermally populated and it, therefore, leads to the appearance and growth of the corresponding emission peaks (for example, the 586 nm, 597 nm, 610 nm, 615 nm, 627 nm, and 632 nm emission peaks, see the black arrows in Fig. 4(b), will appear and gradually increase). On the other hand, the thermal population of the Stark levels (0) of $^1D_2$ is fewer, and the corresponding 612 nm, 626 nm, 636 nm, 645 nm, 648 nm emission peaks decreased rapidly. There are emission peaks from three different Stark energy levels of $^1D_2$ at around 612 nm, and the enhancement of emission peaks from Stark energy levels (2) and (1) is greater than the reduction of the emission peak from Stark energy level (0), so the emission peaks superposed here increased. There are emission peaks from the Stark energy levels (1) and (0) of $^1D_2$ at around 626 nm and 636 nm, and the enhancement of the emission peaks from Stark energy levels (1) is found to be less than the reduction of the emission peaks from the Stark energy level (0); therefore, the emission peaks superposed here decreased slowly. At around 645 nm and 648 nm, there are only emission peaks from Stark energy levels (0), so the emission peaks decrease rapidly. As the temperature further increased from 273 K to 473 K, the thermal quenching induced by high temperature got further enhanced and dominated, so all the emission peaks located within 612–648 nm decreased.

In recent studies, two thermally coupled Stark levels of rare-earth ions can realize optical temperature measurement through the fluorescence intensity ratio (FIR) technology. Following the Boltzmann distribution law, the FIR for the transitions from two thermally coupled levels can be expressed as:[37–39]

$$\mathrm{FIR} = \frac{I_U}{I_L} = B \times \exp\left(-\frac{\Delta E}{KT}\right) \quad (1)$$

with

$$B = \frac{g_U A_U \omega_U}{g_L A_L \omega_L}$$

where I, g, A, and ω represent the integrated intensity of the radiative transition, degeneracy, radiative rate, and transition angular frequency, respectively. The subscript U and L denote the thermally coupled upper and lower levels, respectively. ΔE is the energy gap between the two levels, K is the Boltzmann constant, and T is the absolute temperature.

Here, we focused on the $^1D_{2(2)}$ and $^1D_{2(0)}$ Stark level pair. The 586 nm emission peak is derived from the Stark levels (2) of $^1D_2$, and the 648 nm emission peak is derived from the Stark levels (0) of $^1D_2$. Fig. 6(b) shows the 586 nm and 648 nm emission peaks FIR and relative sensitivity as a function of the absolute temperature. The red curve in the figure is the fitting curve of the experimental data using eqn (1). We can see that the fitting curve matches the experimental data well. The value of $\Delta E/K$ was found to be 977.9 for the fitting curve. Then, the energy gap ΔE between the Stark level (2) and the Stark level (0) can be calculated as 680 cm^{-1}, which is in good agreement with the value of 725 cm^{-1} determined by the PL and PLE spectra. Relative sensitivity (S_r), as one of the vital parameters in practical applications, characterizes the thermometric capability of materials and can be calculated by the following expression:[38,39]

$$S_r = \frac{d(\mathrm{FIR})}{\mathrm{FIR} \times d(T)} = \frac{\Delta E}{KT^2} \quad (2)$$

We can see that the relative sensitivity is only related to ΔE. In our study, the large splitting of the $^1D_2$ brings a high relative sensitivity (9.8% at 100 K).

There are two emission peaks from Stark energy levels (1) and (0) of $^1D_2$ at around 597 nm. Fig. 6(c) shows the 597 nm and 648 nm emission peaks FIR and relative sensitivity as a function of the absolute temperature. Similarly, we used eqn (1) to fit the experimental data and get the red fitting curve. The value of $\Delta E/K$ was determined to be 711.2, and then the energy gap ΔE can be calculated as 494 cm^{-1}, which is 81 cm^{-1} larger than the energy gap 410 cm^{-1} between the $^1D_{2(1)}$ and $^1D_{2(0)}$. This is a reasonable result for the 597 nm emission peak, which is partly derived from the highest Stark level (2) of $^1D_2$.

4. Conclusions

Pr^{3+}-doped $Y_3Si_6N_{11}$ shows a red multi-peaked broad-band emission. The fabricated WLEDs demonstrate that the Pr^{3+} red broad-band can greatly improve the color rendering index. The red emission band was revealed to originate from the combination of the transitions from the large Stark splitting levels of $^1D_2$ to that of $^3H_4$. The diagram of the Pr^{3+} energy level Stark splitting in YSN was achieved. The Stark splitting was 725 cm^{-1} for $^1D_2$ and 930 cm^{-1} for $^3H_4$. Furthermore, a temperature-sensing scheme was proposed based on the temperature-dependent intensity ratios of the emission lines from the thermally coupled Stark levels of the $^1D_2$ state. Relative sensitivities as a function of temperature were studied in the range of 93–473 K. Further, 9.8% relative sensitivity at 100 K was achieved due to the large energy level splitting of $^1D_2$. Thus, our results indicate that the Pr^{3+} red multi-peaked broad-band has application potential for both high color rendering WLEDs and temperature sensing.

Conflicts of interest

The authors declare that there are no conflicts of interest.

Acknowledgements

This work was partially supported by National Key R&D Program of China (Grant No. 2017YFB0403100, 2017YFB0403104), National Natural Science Foundation of China (Grant No. 51772286, 11974346, 11874055, 11904361, 52072361, and 12074373), Youth Innovation Promotion Association CAS No. 2020222, Jilin Province Young and Middle-aged Science and Technology Innovation Leading Talents and Team Projects (20190101001JH). Key Research and Development Program of Jilin Province (20200401050GX). Cooperation project between Jilin Province and Chinese Academy of Sciences (2020SYHZ0013).

Notes and references

1 X. Li, J. D. Budai, F. Liu, J. Y. Howe, J. Zhang, X.-J. Wang, Z. Gu, C. Sun, R. S. Meltzer and Z. Pan, *Light: Sci. Appl.*, 2013, **2**, e50.
2 M. Rajendran, S. K. Samal and S. Vaidyanathan, *J. Alloys Compd.*, 2020, **815**, 152631.
3 R. Devi, K. Singh and S. Vaidyanathan, *J. Mater. Chem. C*, 2020, **8**, 8643.
4 D. Cui, Q. Xiang, Z. Song, Z. Xia and Q. Liu, *J. Mater. Chem. C*, 2016, **4**, 7332–7338.
5 S. Baiqi, H. Jiansheng and Y. Hongpeng, *Adv. Opt. Mater.*, 2019, **7**, 1900319.
6 R. Devi, R. Boddula, J. Tagare, A. B. Kajjam, K. Singh and S. Vaidyanathan, *J. Mater. Chem. C*, 2020, **8**, 11715.
7 G. Li, Y. Tian, Y. Zhao and J. Lin, *Chem. Soc. Rev.*, 2016, **47**, 8688.
8 R. S. Liu and H. D. Nguyen, *J. Mater. Chem. C*, 2016, **4**, 10759.
9 M. Rajendran and S. Vaidyanathan, *Dalton Trans.*, 2020, **49**, 9239.
10 M. Zhao, H. Liao, M. S. Molokeev, Y. Zhou, Q. Zhang, Q. Liu and Z. Xia, *Light: Sci. Appl.*, 2019, **8**, 38.
11 X. Wang, Z. Zhao, Q. Wu, Y. Li and Y. Wang, *J. Mater. Chem. C*, 2016, **4**, 11396–11403.
12 Y. Zhou, E. Song, T. Deng, Y. Wang, Z. Xia and Q. Zhang, *Adv. Mater. Interfaces*, 2019, **6**, 1802006.
13 J. W. Qiao, L. X. Ning, M. S. Molokeev, Y. C. Chuang, Q. Y. Zhang, K. R. Poeppelmeier and Z. G. Xia, *Angew. Chem.*, 2019, **131**, 11645–11650.
14 M. Rajendran and S. Vaidyanathan, *New J. Chem.*, 2020, **44**, 14823.
15 H. S. Kim, K.-i. Machida, T. Horikawa and H. Hanzawa, *J. Alloys Compd.*, 2015, **633**, 97–103.
16 H. Zhong, J. Tang, L. Hao, X. Xu and S. Agathopoulos, *RSC Adv.*, 2016, **6**, 52034–52039.
17 L. Wang, R.-J. Xie, Y. Li, X. Wang, C.-G. Ma, D. Luo, T. Takeda, Y.-T. Tsai, R.-S. Liu and N. Hirosaki, *Light: Sci. Appl.*, 2016, **5**, e16155.
18 C.-W. Yeh, W.-T. Chen, R.-S. Liu, S.-F. Hu, H.-S. Sheu, J.-M. Chen and H. T. Hintzen, *J. Am. Chem. Soc.*, 2012, **134**, 14108–14117.
19 C. Zhang, T. Uchikoshi, R.-J. Xie, L. Liu, Y. Cho, Y. Sakka, N. Hirosaki and T. Sekiguchi, *J. Mater. Chem. C*, 2015, **3**, 7642–7651.
20 Y. Q. Li, J. E. J. V. Steen, J. W. H. V. Krevel, G. Botty, A. C. A. Delsing, F. J. Disalvo, G. D. With and H. T. Hintzen, *J. Alloys Compd.*, 2006, **417**, 273–279.
21 C. Jiang, M. G. Brik, L. Li, L. Li, P. Jie, J. Wu, M. S. Molokeev, K.-L. Wong and M. Peng, *J. Mater. Chem. C*, 2018, **6**, 3016–3025.
22 P. Pust, V. Weiler, C. Hecht, A. Tücks, A. S. Wochnik, A. K. Henß, D. Wiechert, C. Scheu, P. J. Schmidt and W. Schnick, *Nat. Mater.*, 2014, **13**, 891–896.
23 S. You, S. Li, Y. Jia and R. J. Xie, *Chem. Mater.*, 2020, **32**, 3631–3640.
24 H. S. Jang, W. B. Im, D. C. Lee, D. Y. Jeon and S. S. Kim, *J. Lumin.*, 2007, **126**, 371–377.
25 Y. Tang, S. Zhou, X. Yi, D. Hao, X. Shao and J. Chen, *J. Alloys Compd.*, 2018, **745**, 84–89.
26 J. Qiao, J. Zhang, X. Zhang, Z. Hao, Y. Liu and Y. Luo, *Dalton Trans.*, 2014, **43**, 4146–4150.
27 F. B. Xiong, H. F. Lin, Z. Ma, Y. P. Wang, H. Y. Lin, X. G. Meng, H. X. Shen and W. Z. Zhu, *Opt. Mater.*, 2017, **66**, 474–479.
28 T. C. Liu, B. M. Cheng, S. F. Hu and R. S. Liu, *Chem. Mater.*, 2011, **23**, 3698–3705.
29 S. Mahlik, A. Lazarowska, M. Grinberg, T.-C. Liu and R.-S. Liu, *J. Phys. Chem. C*, 2013, **117**, 13181–13186.
30 L.-G. Teoh, M.-T. Tsai, Y.-C. Chang and Y.-S. Chang, *Ceram. Int.*, 2018, **44**, 2656–2660.
31 S. Xin, G. Zhu, B. Wang and Z. Shao, *J. Lumin.*, 2017, **181**, 455–458.
32 X. Yang, J. Liu, H. Yang, X. Yu, Y. Guo, Y. Zhou and J. Liu, *J. Mater. Chem.*, 2009, **19**, 3771.
33 G. Blasse and J. D. Vries, *J. Electrochem. Soc.*, 1967, **114**, 453–454.
34 C. Görller-Walrand and K. Binnemans, *Handb. Phys. Chem. Rare Earths*, 1996, **23**, 121–283.
35 R. Wang, F. Raza, F. Nawaz, H. Fan and Y. Zhang, *J. Lumin.*, 2020, **223**, 117245.
36 D. S. Sun, L. L. Zhang, Z. D. Hao, X. Zhang, G. H. Pan, H. J. Wu, Y. S. Luoa, S. He, H. F. Zhao and J. H. Zhang, *Dalton Trans.*, 2018, **47**, 16723–16728.
37 G. Yan, Y. S. Wang, H. Lin, J. Xu and F. Huang, *Sens. Actuators, B*, 2017, **243**, 137–143.
38 X. Tian, C. Wang, J. Wen, S. Lian, C. Ji, Z. Huang, Z. Chen, H. Peng, S. Wang, J. Li, J. Hu and Y. Peng, *J. Lumin.*, 2019, **214**, 116528.
39 C. D. Brites, P. P. Lima, N. J. Silva, A. Millan, V. S. Amaral, F. Palacio and L. D. Carlos, *Nanoscale*, 2012, **4**, 4799–4829.